Energy & Environmental Science

ROYAL SOCIETY OF CHEMISTRY

PAPER

View Article Online
View Journal | View Issue

Cite this: *Energy Environ. Sci.*, 2022, **15**, 5229

Molten salt electrolytes for electrochemical capacitors with energy densities exceeding 50 W h kg^{-1}†

Kuangyu Wang, ‡[a] Ziyao Chen,‡[a] Kai Liu,*[b] Cheng Yang,[c] Haitian Zhang,[d] Yulong Wu,[a] Yuanzheng Long,[a] Hanlin Liu,[a] Yang Jin,[e] Meicheng Li[b] and Hui Wu*[a]

Received 21st June 2022,
Accepted 15th September 2022

DOI: 10.1039/d2ee01969h

rsc.li/ees

Electrochemical capacitors (ECs) are promising energy storage devices due to their superior power density and outstanding cycling stability. The development of EC electrolytes is of key importance to further promote their energy density and overall performance. Herein, we report molten salts as a new electrolyte category for ECs with superior performance. The molten-salt-based EC (MS-EC) device assembled with an $AlCl_3$–NaCl–LiCl electrolyte and activated carbon electrodes provided an ultrahigh energy density of 50.4 W h kg^{-1} at a power density of 1.1 kW kg^{-1} at 125 °C. The energy storage process is clarified to follow a physisorption–chemisorption combined mechanism originating from electrolyte nanoconfinement effects. MS-ECs also demonstrate high cycling stability (99.8% capacitance retention after 10 000 cycles), low cost, and capability for long-duration energy storage (over 90% voltage retention after 25 days at room temperature). This study provides insights into the research on energy storage mechanisms and broadens the application field of ECs.

Broader context

Electrochemical capacitors (ECs) are characterized by high power density, long cycle life, and low maintenance costs. As a result, they have essential application prospects for high-rate energy harvesting, storage, and delivery. A major concern of EC devices is their relatively low energy densities compared with batteries. Electrolyte materials, which can be classified into various types including aqueous, organic, and ionic liquid systems, fundamentally affect the device performance. However, aqueous electrolytes are limited by their narrow electrochemical windows, while the ionic conductivity of organic and ionic liquid electrolytes is relatively low. Herein, molten salts with high ionic conductivity, wide electrochemical windows, low raw material costs, and high safety are reported as a new electrolyte category for high-performance ECs. Molten-salt-based ECs (MS-ECs) with commercial activated carbon electrodes deliver ultrahigh energy densities of over 50 W h kg^{-1}. The energy storage process of MS-ECs is revealed to follow a physisorption–chemisorption combined mechanism originating from the electrolyte nanoconfinement effect. Moreover, by utilizing the ion insulation characteristics of the molten salt in the solid state, we propose that long-duration energy storage can be realized by cooling down the electrolyte. The design of the MS-EC system not only improves the device energy densities but also has a far-reaching scientific value for research on energy storage mechanisms.

[a] *State Key Lab of New Ceramics and Fine Processing, School of Materials Science and Engineering, Tsinghua University, Beijing 100084, P. R. China. E-mail: huiwu@tsinghua.edu.cn*

[b] *State Key Laboratory of Alternate Electrical Power System with Renewable Energy Sources, School of New Energy, North China Electric Power University, Beijing 102206, P. R. China. E-mail: liukai21@ncepu.edu.cn*

[c] *Center for Advanced Mechanics and Materials Applied Mechanics Laboratory, Department of Engineering Mechanics, Tsinghua University, Beijing 100084, P. R. China*

[d] *Institute of Nuclear and New Energy Technology, Tsinghua University, Beijing 100084, P. R. China*

[e] *Research Center of Grid Energy Storage and Battery Application, School of Electrical Engineering, Zhengzhou University, Zhengzhou 450001, P. R. China*

† Electronic supplementary information (ESI) available. See DOI: https://doi.org/10.1039/d2ee01969h

‡ These authors contributed equally to this work.

Introduction

Electrochemical capacitors (ECs) have important application prospects for high-rate energy harvesting, storage, and delivery because of their high power density, long cycle life, and low maintenance costs.[1,2] ECs are a critical component of smart grids to improve the reliability of the electrical energy distribution and facilitate the employment of renewable energy sources.[3–5] In addition, they have been widely applied in the oil and gas industry, hybrid electric vehicles, and the military and aerospace industry.[6–8] Electrolytes are an essential component in ECs and have fundamental effects on the device performance.[6] In general, electrolytes for ECs can be classified

into three types: aqueous, organic, and ionic liquid electrolytes.[9] Aqueous electrolytes commonly exhibit the advantages of high ionic conductivity (up to 1 S cm^{-1}), low cost, ease of handling, and nonflammability.[10] However, high energy density is hard to achieve for ECs based on aqueous electrolytes due to the narrow electrochemical windows of these aqueous solutions.[11] ECs based on organic or ionic liquid electrolytes currently dominate the commercial market because of their wider operational potential windows.[12] Nevertheless, the lower ionic conductivity and higher viscosity of non-aqueous electrolytes may hinder ion migration and penetration, leading to lower specific capacitances of the electrode and inferior rate capability.[10] Furthermore, safety concerns related to the flammability, volatility, and toxicity of organic electrolytes and the high prices of ionic liquid electrolytes are imminent problems that need to be solved.[12,13]

Inorganic molten salts have been investigated as electrolyte materials for high-temperature batteries.[14–17] They consist of ions with various valences, which are in direct contact due to the absence of solvents.[18] The high mobility of the ions results in high ionic conductivity and superior rate capability of the energy storage devices.[19] As a result, we propose that molten salt electrolytes may provide new opportunities to improve the energy and power densities of ECs. Additionally, molten salt electrolytes are characterized by wide electrochemical windows, low raw material costs, non-flammability, and non-toxicity.[20,21]

In practice, multicomponent salt mixtures are prepared to reduce the melting points and broaden the operating temperature windows of the electrolyte systems, which is essential for smart grid systems.[17,22,23] It is worth noting that the temperature difference inside the module should be less than 5 °C for room-temperature ECs.[24] The required thermal management systems may lead to increased weight and cost.[24–26] Moreover, applying a molten salt electrolyte enables the corresponding EC device to operate in harsh application environments, including deep reservoirs in the oil and gas industry (up to 200 °C), high-temperature regions around internal combustion engines or fuel cells in hybrid electric vehicles (up to 300 °C), and even planetary surfaces for space exploration (up to 480 °C).[27–29]

Herein, we propose high-performance ECs constructed with an $AlCl_3$–NaCl–LiCl molten salt electrolyte and activated carbon (AC) electrodes. The energy storage process of the molten-salt-based EC (MS-EC) was identified to follow a physisorption–chemisorption combined mechanism, which was attributed to the unique properties of the molten salt electrolyte confined in the nanopores of the electrode. The electrode capacitance was significantly higher when using the $AlCl_3$–NaCl–LiCl electrolyte (419 F g^{-1} at 125 °C) compared to other non-aqueous electrolytes (typically smaller than 150 F g^{-1}). MS-EC devices delivered an ultrahigh energy density of 50.4 W h kg^{-1} at a power density of 1.1 kW kg^{-1} at 125 °C compared to around 15.0, 25.0, and 35.0 W h kg^{-1} for ECs based on aqueous, organic, and ionic liquid electrolytes, respectively. The self-discharge of the devices at different temperatures was also systematically analyzed, and long-duration energy storage (25 days) with over 90% voltage retention was realized by cooling down the electrolyte to its solid state. In addition, molten salts with different compositions, melting points, and electrochemical windows were successfully applied as electrolytes, proving the universal application of suitable molten salts for EC systems.

Results

MS-EC configuration and electrolyte properties

Fig. 1a displays the configuration of the MS-EC device. Both electrodes were fabricated from commercial AC powders with Mo meshes and Ta wires as current collectors. A glass fiber separator was placed between the electrodes to prevent short circuits, and a stainless-steel vessel was filled with the solid $AlCl_3$–NaCl–LiCl electrolyte. After being sealed for gas tightness, the device was heated to a specific temperature for testing.

The employed AC powders possessed particle sizes on the micron scale with mainly non-crystalline structures (Fig. S1, ESI†). They exhibited a specific surface area of 2070 m^2 g^{-1} with pore width diameters concentrated in the range of 0.5–1.5 nm (Fig. S2, ESI†). According to the X-ray photoelectron spectroscopy (XPS) results, four characteristic peaks were centered at 284.5, 285.7, 287.2, and 290.1 eV in the C 1s spectrum, representing C–C/C═C, C–N, C═O, and O–C═O as the present carbon species, respectively (Fig. S3, ESI†).[30] To determine the extent of graphitization, Raman spectra and X-ray diffraction (XRD) patterns were recorded. Both the D band ($\sim$1327 cm^{-1}) and G band ($\sim$1580 cm^{-1}) were present in the Raman spectrum with a relative intensity ratio (I_D/I_G) of 1.01 (Fig. S4, ESI†). As seen in Fig. S5 (ESI†), two peaks at 2θ = 26.6° and 43.5° were observed in the XRD pattern, which corresponded to the (002) and (100) planes of graphitic carbon and indicated structures of graphitic stacking. Freestanding AC electrodes with different thicknesses were fabricated, and the AC particles adhered together according to the scanning electron microscopy (SEM) images (Fig. S6 and S7, ESI†).

The $AlCl_3$–NaCl–LiCl salt mixture was prepared as the electrolyte with a molar ratio of 0.6 : 0.2 : 0.2, which is close to the eutectic composition.[31] The melting point of the electrolyte system was as low as 82 °C (Fig. S8, ESI†), allowing MS-ECs to be operated within a wider temperature range. Peaks of $AlCl_3$, $NaAlCl_4$, and $LiAlCl_4$ were observed in the XRD patterns of the electrolyte in the solid state (Fig. 1b). Fig. 1c demonstrates the Raman spectra of the electrolyte at 25 and 125 °C. The peak at 349 cm^{-1} was assigned to the normal vibration modes of the tetrahedral moiety of "$AlCl_4$", while the peak at 305 cm^{-1} corresponded to $AlCl_3$ in the solid state.[32] Broadening of the Raman peaks at 125 °C indicated a higher degree of structural disorder of the electrolyte in the liquid state, and the three peaks located at 316, 365, and 518 cm^{-1} were attributed to $AlCl_4^-$, $Al_2Cl_7^-$ and Al_2Cl_6, respectively.[33–35]

For further research on the microstructure of the molten salt system, molecular dynamics (MD) simulations were performed. Fig. 1d demonstrates a representative simulation snapshot, in which Na^+ and Li^+ were uniformly dispersed, and no obvious

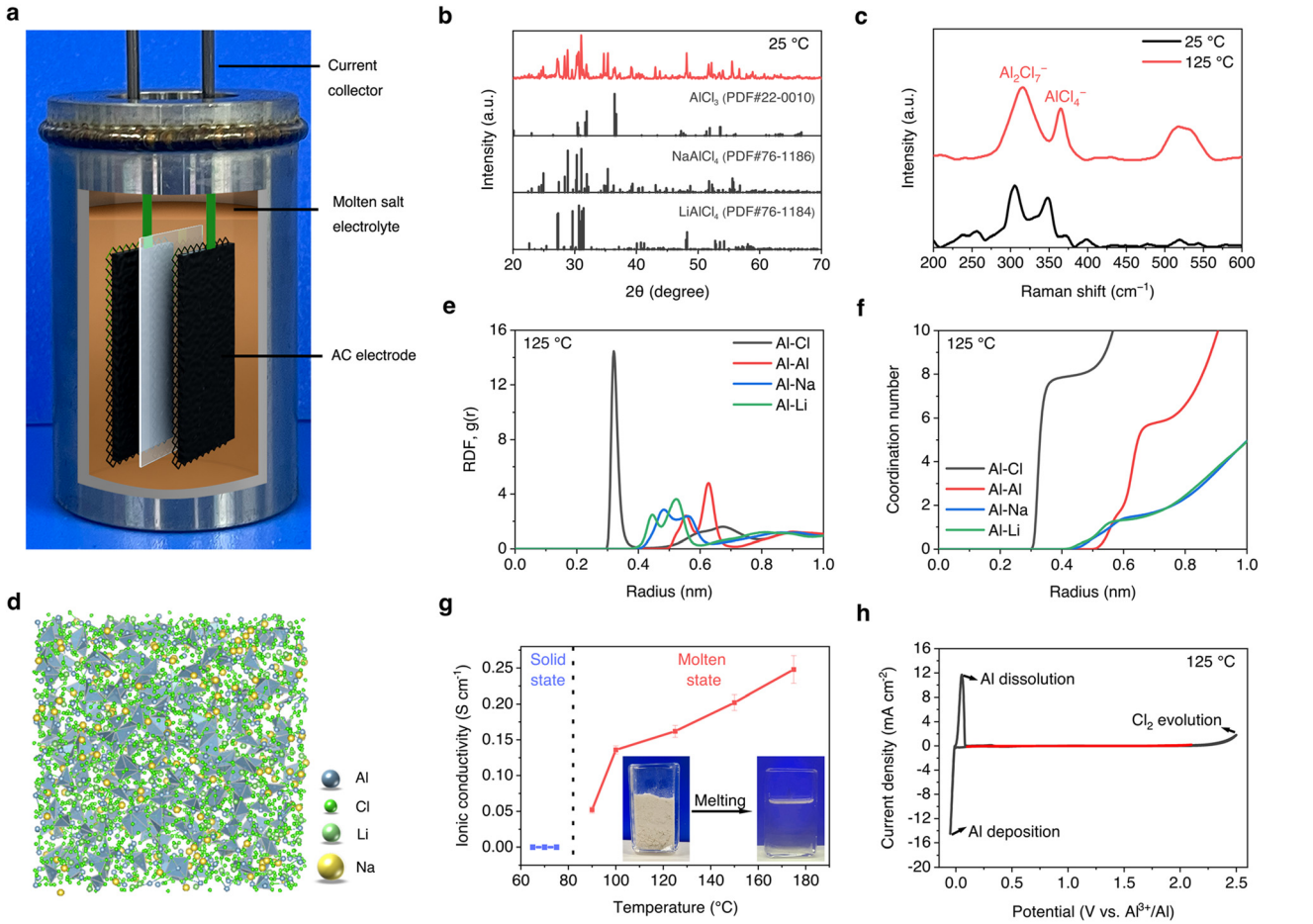

Fig. 1 MS-EC configuration and electrolyte properties. (a) Schematic diagram of the MS-EC device. (b) XRD pattern of the $AlCl_3$–NaCl–LiCl electrolyte at 25 °C. (c) Raman spectra of the $AlCl_3$–NaCl–LiCl electrolyte at 25 and 125 °C. (d) Representative simulation snapshot of the $AlCl_3$–NaCl–LiCl system at 125 °C calculated using MD simulations. (e) RDFs and (f) coordination number integral curves of the Al–Cl, Al–Al, Al–Na, and Al–Li ion pairs of the $AlCl_3$–NaCl–LiCl system at 125 °C calculated using MD simulations. (g) Ionic conductivities at different temperatures and digital photos of the $AlCl_3$–NaCl–LiCl electrolyte in the solid and molten states. (h) CV curves of the $AlCl_3$–NaCl–LiCl electrolyte in the voltage ranges of −0.05 to 2.5 V (black) and 0.1–2.1 V (red) at 125 °C at a scan rate of 10 mV s^{-1}.

agglomeration was observed. Statistical results of the radial distribution functions (RDFs) of some ion pairs in the system are demonstrated in Fig. 1e. The first peak radius of the Al–Cl ion pair was significantly smaller than those of Al–Al, Al–Na, and Al–Li ion pairs, which means the Cl^- ions mostly gathered around Al^{3+} ions to form complexes ($AlCl_4^-$, $Al_2Cl_7^-$, *etc.*). The existence of $Al_2Cl_7^-$ ions was confirmed by the Al–Al ion pair RDF, from which two peaks with corresponding radii of 0.56 and 0.63 nm could be seen. The radius of the left peak was 0.08 nm smaller than the length of two Al–Cl bonds, indicating pairs of Al^{3+} ions linked by common Cl^- ions.[36] Furthermore, the coordination number integral curves of the Al–Li and Al–Na ion pairs showed no apparent differences, which can be attributed to their similar ion diameters (Fig. 1f).

The ionic conductivity of the $AlCl_3$–NaCl–LiCl electrolyte was tightly correlated with temperature. In Fig. 1g, when the temperature was below the melting point of the electrolyte, the ionic conductivity was nearly zero. The electrolyte turned into a colorless transparent melt and exhibited an ionic conductivity of 0.05 S cm^{-1} at 90 °C. The conductivity further increased to 0.14, 0.16, 0.20, and 0.25 S cm^{-1} at 100, 125, 150, and 175 °C, respectively. Cyclic voltammetry (CV) tests were performed at a scan rate of 10 mV s^{-1} to determine the electrochemical window of the electrolyte (Fig. 1h). Al deposition started at −0.01 V *vs.* Al^{3+}/Al with a corresponding anodic peak at 0.06 V, while the reaction of the chlorine gas evolution occurred when the potential was higher than 2.2 V. Negligible side reactions were observed in the potential range of 0.1–2.1 V *vs.* Al^{3+}/Al.

Energy storage mechanisms

CV tests were performed to evaluate the electrochemical performance of the AC electrode in the $AlCl_3$–NaCl–LiCl molten salt electrolyte (Fig. 2a). The calculated specific capacitance of the electrode was 419 F g^{-1} at a scan rate of 5 mV s^{-1}, which decreased to 209 F g^{-1} at a scan rate of 100 mV s^{-1}. The CV curves presented nearly rectangular shapes with a few broad redox peaks, indicating the occurrence of faradaic reactions

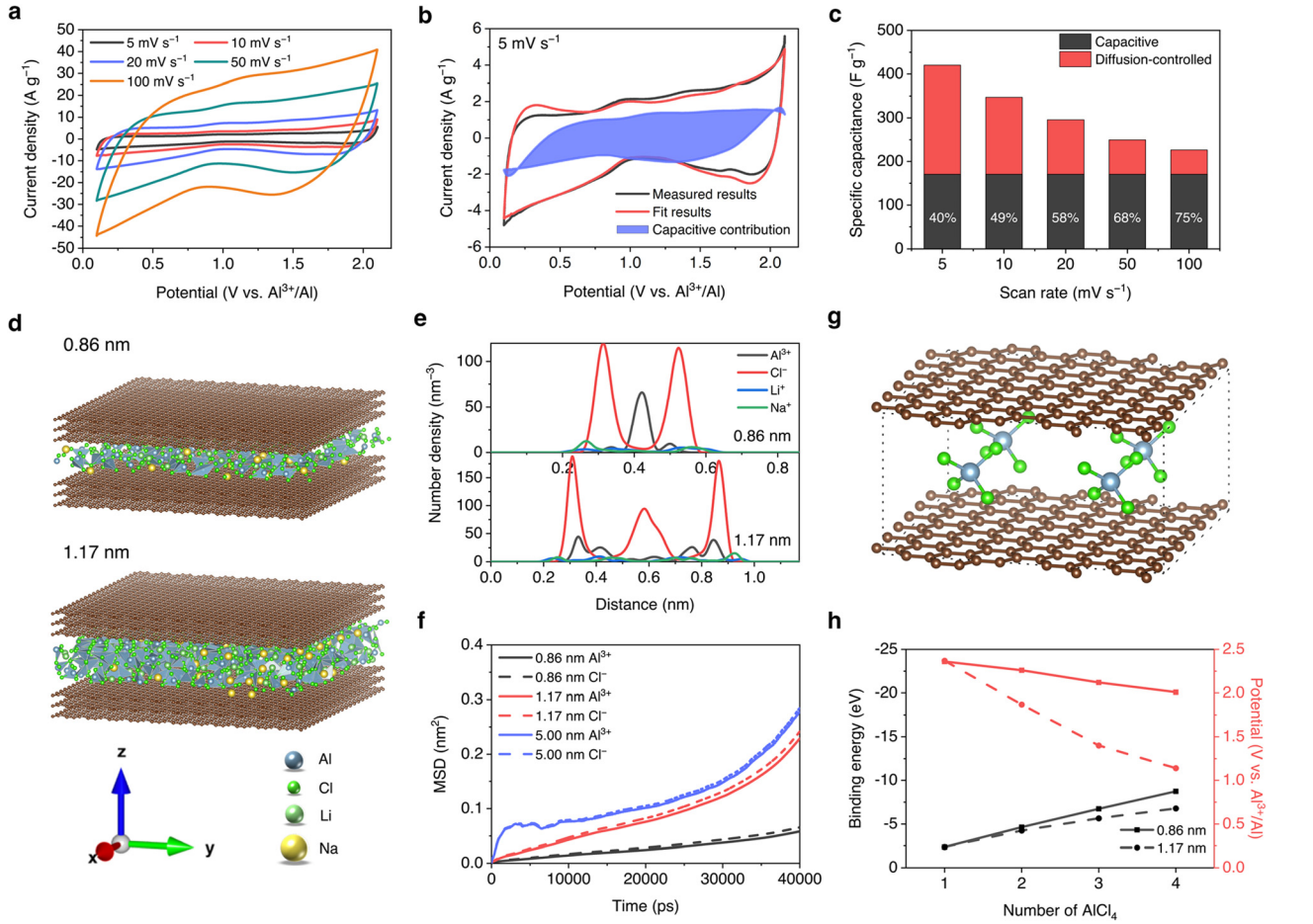

Fig. 2 Energy storage mechanisms of the AC electrode. (a) CV curves of the AC electrode in the $AlCl_3$–NaCl–LiCl electrolyte at 125 °C and different scan rates. (b) CV curves with experimental and fitted results at 5 mV s^{-1}. The blue area represented the capacitive contribution. (c) Capacity contribution ratios of the capacitive and diffusion-controlled mechanisms at different scan rates. (d) Representative simulation snapshots of the $AlCl_3$–NaCl–LiCl system confined in graphene slit pores with widths of 0.86 and 1.17 nm at 125 °C calculated using MD simulations. (e) Number density profiles along the *z*-direction and (f) MSDs of Al^{3+} and Cl^- ions of the $AlCl_3$–NaCl–LiCl system confined in graphene slit pores with widths of 0.86 and 1.17 nm at 125 °C calculated using MD simulations. (g) Schematic representations of the optimized structures of the graphene slit pore with a width of 0.86 nm with 4 intercalated $AlCl_4$ calculated using DFT simulations. (h) Binding energies and intercalation potentials of the optimized structures of graphene slit pores with widths of 0.86 and 1.17 nm with 1, 2, 3, and 4 intercalated $AlCl_4$ calculated using DFT simulations.

(Fig. 2b and Fig. S9, ESI†). The following equation was used to quantify capacitive and diffusion-controlled contributions to the total current.[37]

$$i(V) = k_1 v + k_2 v^{1/2} \quad (1)$$

where $i(V)$, v, $k_1 v$, and $k_2 v^{1/2}$ represent the total current, scan rate, capacitive current, and diffusion-controlled current, respectively. By plotting $v^{1/2}$ *vs.* $i/v^{1/2}$, k_1 and k_2 can be calculated.[37] As shown in Fig. 2b and c, the capacitive contribution represented by the blue area accounted for 40% of the total charge storage capacity at a scan rate of 5 mV s^{-1}. The value increased with the scan rate, reaching 75% at a scan rate of 100 mV s^{-1} (Fig. 2c and Fig. S10, ESI†).

The energy storage process of ECs is related to electrostatic adsorption or faradaic reactions at/near the electrode surface.[2] The electrolyte confined in the nanopores of the AC electrode typically demonstrates different local liquid structures and ion dynamics from the bulk state, which further influences the macroscopic capacitance and electrical resistance of the device.[38] As a result, the nanoconfinement of the molten salt electrolyte was studied to clarify the origin of the high specific capacitance of the AC electrode in the molten salt electrolyte.

MD simulations were conducted based on a slit pore geometry, which means the ions were supposed to be confined in the direction perpendicular to two groups of adjacent graphene sheets (*z*-direction). The width of the pore was represented by the minimum surface-to-surface distance between the graphene sheets. Fig. S11 (ESI†) demonstrates the microstructure of the molten salt confined in a wide slit (5.00 nm). The ion number density along the *z*-direction exhibited an oscillatory behavior, indicating layered stacking of the ions (Fig. S12, ESI†). The maxima in the local density were observed close to the surface of the graphene sheets, and the density fluctuations diminished away from the surfaces. In other words, the ion arrangement in the middle region was close to that in the bulk state, while obvious deviations were observed near the graphene

surfaces, which can be attributed to the ion–host interactions. Then the widths of the slit were determined as 1.17 and 0.86 nm according to the measured pore size distributions of the employed AC powders. As seen in Fig. 2d and e, bilayer and monolayer ion structures were observed in the pores with widths of 1.17 and 0.86 nm, respectively. In particular, Al^{3+} ions gathered around the middle region in the 0.86 nm-wide pore, while Na^+ and Li^+ were mainly closer to the graphene sheets. Moreover, the two symmetrical peaks of the density profile of Cl^- indicated ordered orientations of the chloroaluminate ions. These results provided an atomic scale explanation for the experimentally discovered high capacitance of the AC electrode. For the electrolyte in the bulk state, the ion structure mainly follows coulombic ordering, which means each ion is surrounded by successive shells of opposite charge.[39] However, the disruption of the bulk order was observed when the molten salt was under specific confinement microenvironments. Such an effect may induce increased cation pairs and anion pairs and further help the formation of dense double-layer structures during charging and the achievement of high capacitance.[40,41]

The mean square displacements (MSDs) of the ions are a vital parameter in evaluating the mobility of the confined ions. Ion dynamics were more sluggish when the slit pore was narrower, which is consistent with the results of nanoconfined ionic liquids (Fig. 2f).[38,42,43] Na^+ and Li^+ showed higher mobility than Al^{3+} and Cl^- probably because of their smaller ion sizes compared with the chloroaluminate ions (Fig. S13, ESI†). Experimental results helped to better understand confined ion dynamics. The AC powders with confined $AlCl_3$–NaCl–LiCl molten salt (MS@AC) could be prepared *via* a simple post-impregnation method. The AC powders were heated with the molten salt, and then the sample was cooled down to room temperature and washed with deionized water to remove the surface adsorbed molten salts. The removal of the surface adsorbed electrolyte after washing was verified by SEM (Fig. S14, ESI†). The energy-dispersive X-ray (EDX) spectra and argon adsorption–desorption isotherms of the MS@AC powders indicated that the pores were occupied by the solidified electrolyte (Fig. S15, ESI†). The peaks of the molten salt could also be observed in the XRD pattern (Fig. S16, ESI†). Since the molten salt has lower viscosity and higher conductivity than ionic liquids in the bulk state, it demonstrated better wettability over the surfaces of the nanopores of the electrode,[44] which is essential for the high-power performance of MS-ECs.

AC electrodes typically store electrical charge in ECs *via* the formation of electric double-layers, meaning that the capacitive contribution dominates.[45,46] However, the capacitance contributions from faradaic reactions were considerable in the MS-ECs. Moreover, the melting point of the electrolyte confined in the nanopores showed a decrease of 11 °C (Fig. S17, ESI†). Both phenomena could be caused by the strong ion–host interactions under nanoconfinement.[41] The possible faradaic reaction is listed as follows.

$$C_n + AlCl_4^- \rightleftharpoons C_n[AlCl_4] + e^- \quad (2)$$

where n is the molar ratio of carbon atoms to intercalated anions, which is dependent on multiple parameters, including the pore structure and the electrode potential. The occurrence of the intercalation reactions was further verified by density functional theory (DFT) simulations based on graphene slit pores (Fig. 2g and Fig. S18, ESI†). The pore widths were determined as 0.86 and 1.17 nm for consistency with the MD simulations. As seen in Fig. 2h, the calculated binding energies of $AlCl_4$ and graphene were negative for both models, and the values decreased with the number of intercalated $AlCl_4$, suggesting that the reactions were favorable at higher $AlCl_4$ concentrations.[47] The intercalation potentials for the pores with widths of 0.86 and 1.17 nm varied in the ranges of 2.01–2.36 V and 1.14–2.37 V, respectively, which were in agreement with the experimentally reported values. The intercalation potentials were higher in the narrower slit pore. Considering the pores of the employed AC were distributed in the range of 0.5–1.5 nm, the corresponding CV curves would demonstrate potential-dependent current features with broad peaks.

To conclude, the energy storage process of the AC electrode in the $AlCl_3$–NaCl–LiCl molten salt electrolyte followed a physisorption–chemisorption combined mechanism, which originated from the unique structures and properties of the molten salt electrolyte confined in the nanopores of the electrode. On the one hand, altered local ion structures under specific nanoconfinement conditions were observed, which may contribute to the formation of a denser double-layer structure and higher capacitive capacitances. On the other hand, DFT simulations indicated that intercalation reactions of $AlCl_4^-$ into the nanopores of the AC electrode were favorable. As a result, the AC electrode exhibited considerable diffusion-controlled capacitances in the molten salt, promoting the preparation of high-energy-density EC devices.

Electrochemical performance

To estimate the electrochemical performance of the full device, MS-ECs with AC electrodes were assembled and tested. The current densities of the MS-EC devices were calculated based on the mass of AC in both electrodes. According to Fig. S19 (ESI†), the device failed to operate at 75 °C, illustrating the necessity of operating temperatures higher than the melting point of the electrolyte. Fig. S20 (ESI†) shows that negligible capacity was obtained in the device with bare Mo meshes on both electrodes, excluding the influence of side reactions.

The theoretical operational voltage of an EC is determined by the electrochemical window of the electrolyte. However, if the two electrodes do not reach their respective limit potentials simultaneously during the charging process, decomposition of the electrolyte may occur even when the EC device operates within the theoretical voltage range.[48,49] For MS-ECs, chlorine gas production and aluminum deposition during the decomposition of the electrolyte may affect the mechanical integrity of the electrode and cause capacitance decay.[50] As a result, electrode mass balancing is necessary. Asymmetric MS-ECs with different cathode-to-anode mass ratios (M_+/M_-) were assembled according to Table S1 (ESI†). Fig. 3a and Fig. S21 (ESI†) show the galvanostatic charge–discharge (GCD) curves of the MS-ECs at 125 °C and different current densities. The device

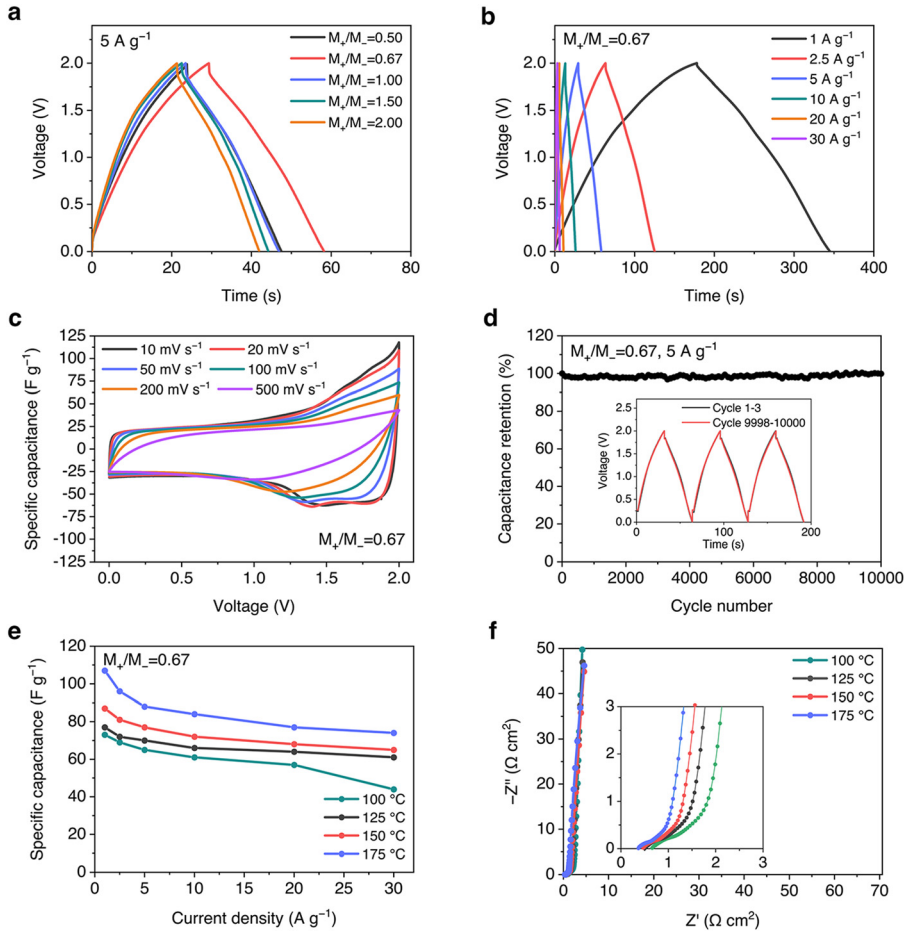

Fig. 3 Electrochemical performance of the MS-EC. (a) GCD curves of the MS-ECs with different M_+/M_- values at 125 °C and a current density of 5 A g^{-1}. (b) GCD curves of the MS-EC at 125 °C and different current densities. (c) CV curves of the MS-EC at 125 °C and different scan rates. (d) Cycling performance of the MS-EC at a current density of 5 A g^{-1} and GCD curves of the first and last 3 cycles. (e) Specific capacitances of the MS-EC at different temperatures and current densities. (f) EIS measurements of the MS-EC (Device #1) at different temperatures.

with an M_+/M_- value of 0.67 achieved the highest specific capacitance at all the current densities and demonstrated good rate capability with 79% capacitance retention when the current densities increased from 1 A g^{-1} (with a capacitance of 77 F g^{-1}) to 30 A g^{-1} (with a capacitance of 61 F g^{-1}) (Fig. 3b). Based on these results, M_+/M_- was fixed at 0.67 in the following tests.

Fig. 3c and Fig. S22 (ESI†) present the CV curves of the MS-EC at 125 °C. In the voltage range of 0–1.0 V, the specific capacitance remained almost unchanged at different scan rates. In contrast, a decrease in capacitance with the scan rate was observed in the voltage range of 1.0–2.0 V, further verifying the occurrence of the faradaic reactions reported in the previous section.

To assess the cycling stability of the MS-EC, a repeated GCD test was performed at 125 °C and a current density of 5 A g^{-1} (Fig. 3d). The device presented exceptional stability with negligible capacitance loss (99.8% capacitance retention) after 10 000 cycles. Furthermore, the GCD curves of the first and last three cycles remained nearly unchanged. The cyclability of the device was confirmed by characterization of the electrode and the electrolyte. According to the SEM images, the AC electrode maintained mechanical stability after cycling (Fig. S23, ESI†). Meanwhile, the XRD patterns, XPS spectra, Raman spectra, and elemental contents of the electrolyte did not exhibit apparent changes (Fig. S24–S26 and Table S2, ESI†).

The electrochemical performance of the MS-EC was then evaluated at different operating temperatures. As shown in Fig. 3e and Fig. S27 (ESI†), higher specific capacitances were achieved at elevated temperatures. For example, the capacitance increased from 73 to 107 F g^{-1} while the IR drop decreased from 23 to 18 mV at a current density of 1 A g^{-1} when the temperature rose from 100 to 175 °C. Electrochemical impedance spectroscopy (EIS) measurements of four MS-EC devices confirmed the comprehensive performance improvement of the MS-ECs at elevated temperatures (Fig. 3f and Fig. S28, ESI†). All the devices demonstrated decreased equivalent series resistance (ESR), interfacial resistance (R_{int}), and relaxation time constant at higher temperatures (Table S3, ESI†), which reflected the higher electrolyte conductivity and the faster ion migration process across the electrolyte and electrode interfaces.[51]

Self-discharge performance

Self-discharge is a non-negligible parameter for ECs.[52] Four different self-discharge mechanisms (ohmic leakage,

activation-control, diffusion-control, and charge redistribution (CR)) were proposed by Conway *et al.*[53] Combined effects of multiple mechanisms may occur in practical systems.[54] Fig. 4a displays the self-discharge profiles of the MS-EC at different temperatures. The open-circuit voltages of the device were 1.87, 1.72, 1.63, 1.60, and 1.51 V at 90, 100, 125, 150, and 175 °C after 3 h, respectively. The increased self-discharge rate with the operating temperature can be commonly attributed to an enhanced electrochemical activity within the system. For further quantitative assessments, the relation between voltage loss during the self-discharge process (V_{loss}) and time (t) can be expressed as follows.[55]

$$V_{loss} = A\sqrt{t} + B\ln(t+\tau) \quad (3)$$

where A is the diffusion parameter, while B and τ are related to the activation-controlled and CR mechanisms since the mathematical treatments of both mechanisms are the same. Ohmic leakage was not considered to occur in this system. According to the two terms in eqn (3), the voltage loss of the device at different temperatures was divided into two parts (Fig. S29, ESI†), one related to the square root of time (blue dashed line) and one to the logarithm of time (green dashed line). To distinguish the effects of the activation-controlled and CR mechanisms, self-discharge tests with different holding times were conducted. In Fig. S30 (ESI†), the voltage decay decreased with the holding time at 125 °C from an initial 0.41 V for no holding to 0.31 V for a 4 hour holding. It has been reported that charge distributions on porous carbon electrodes are tightly correlated with the holding time, while the activation-controlled mechanism generally demonstrates no changes.[55] As a result, the part of the voltage loss obeying the logarithmic law with time was mainly related to the CR mechanism.

As seen in Fig. 4b and Fig. S31 (ESI†), self-discharge rates related to the CR and diffusion-controlled mechanisms were higher at elevated temperatures. The voltage losses correlated with the diffusion-controlled and CR mechanisms were 0.06 and 0.07 V at 90 °C, respectively, while the values increased to 0.25 and 0.24 V at 175 °C (Fig. 4b). Under open-circuit conditions, the CR mechanism drives the charged states of the electrode toward equilibrium by rearranging the charges from higher to lower surface charge density.[55] Consequently, faster ion diffusion at elevated temperatures may accelerate voltage decay. Meanwhile, the faster kinetics of the deintercalation

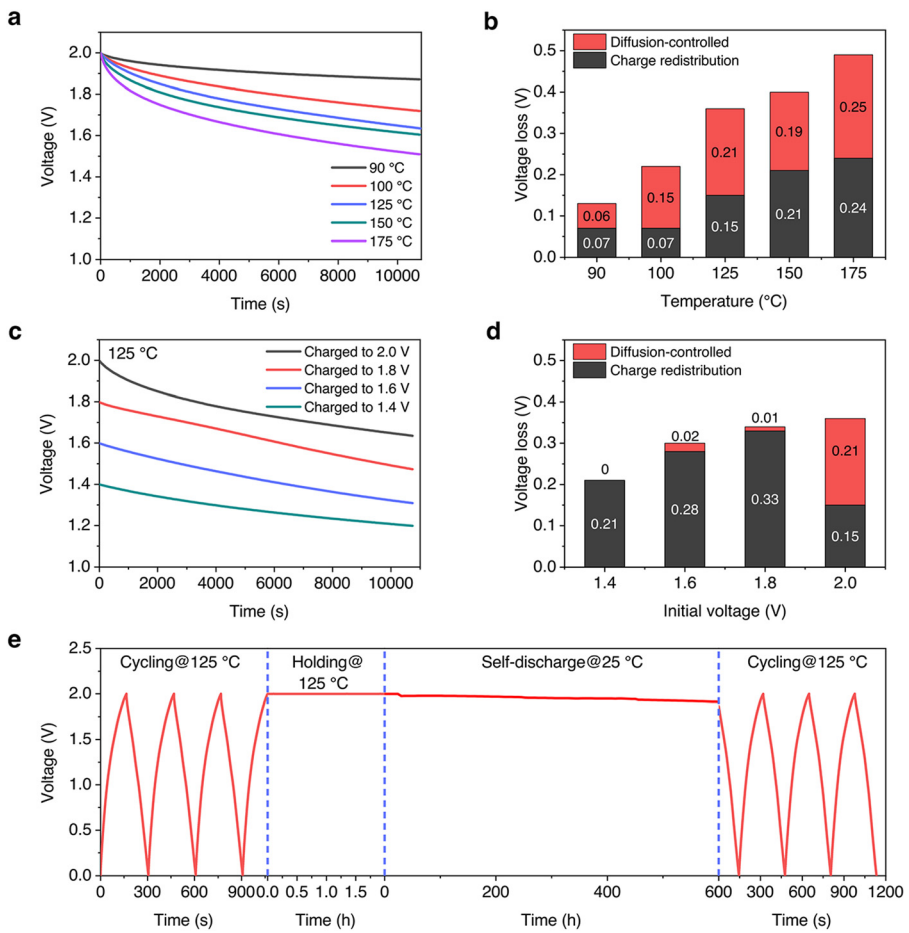

Fig. 4 Self-discharge tests of the MS-EC. (a) Self-discharge profiles and (b) voltage losses from charge redistribution and diffusion-controlled mechanisms at different temperatures. (c) Self-discharge profiles and (d) voltage losses from charge redistribution and diffusion-controlled mechanisms at different initial voltages. (e) Long-duration self-discharge tests.

reactions at higher temperatures may lead to larger energy loss related to the diffusion-controlled mechanism.[56]

For further understanding of the self-discharge process of the MS-EC, tests were performed on the devices with different initial voltages (Fig. 4c). In Fig. 4d, when the initial voltage was 2.0 V, the CR and diffusion-controlled mechanisms contributed to 40% and 60% of the voltage loss, respectively. In contrast, when the initial voltage was below 1.8 V, the CR mechanism was the dominant factor of self-discharge. This phenomenon was consistent with the CV measurement of the device (Fig. 3c), confirming the potential-dependent feature of the energy storage mechanism of the electrode.

Electrolyte additives and modified separators have been applied to reduce the self-discharge rate for a specific EC system.[57,58] However, both methods resulted in increased raw material costs and decreased electrolyte conductivity, which may influence the power densities of the devices.[59] Our MS-EC design provided a possibility for long-duration energy storage. Since the electrolyte was ionically insulating at ambient temperature, self-discharge was significantly suppressed. As seen in Fig. 4e, an open-circuit voltage retention of 1.91 V after 25 days was achieved, and the device functioned normally after being heated to the operating temperature.

Based on the results above, the working conditions of the MS-EC can be moderated according to the practical application environment. For MS-ECs integrated into smart grids, when the device does not need to output electric energy in the next few hours, the temperature can be adjusted to around 90 °C, where the self-discharge rate of the device is slower than that of the room-temperature EC devices. Meanwhile, the device can be quickly heated to a higher temperature with a small amount of energy consumed in the heating process (Table S4, ESI†). Moreover, for the MS-ECs operating under harsh environments, the energy can be stored for an extended period by maintaining a temperature below the melting point of the electrolyte. At the same time, the external heat sources can provide the energy required for the heating and operation of the device.

Comparisons of EC systems with different electrolytes

The ECs based on the $AlCl_3$–NaCl–LiCl molten salt electrolyte demonstrated better all-around electrochemical performance than those based on other electrolytes. The energy and power densities of the MS-EC systems, which were calculated based on the active material mass of the AC electrodes, are revealed in Fig. 5a.[60–65] Ultrahigh energy densities of 50.4, 44.7, 42.0, 35.5, 26.3, and 19.7 W h kg^{-1} were achieved at power densities of 1.1, 2.8, 5.2, 9.8, 17.2, and 22.8 kW kg^{-1} at 125 °C, respectively. A further performance improvement was observed at 175 °C, with the energy density exceeding 60.0 W h kg^{-1} at a power density of 1.0 kW kg^{-1}. The energy density depends on the device operating voltage and the electrode capacitance (eqn (4)).[63] The MS-EC can be operated in a relatively wide voltage range of 0–2.0 V, with ultrahigh electrode capacitances achieved following the physisorption–chemisorption combined energy storage mechanism. As a result, MS-ECs have the

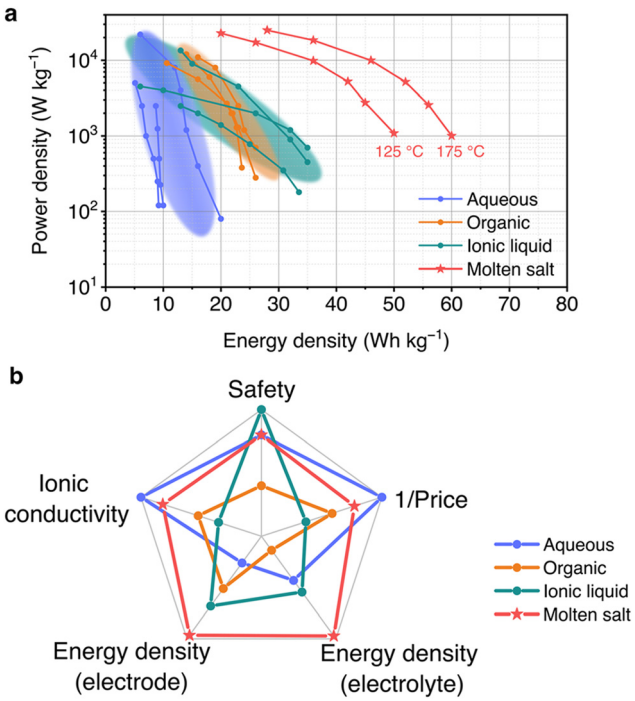

Fig. 5 Comparisons of EC systems based on the molten salt electrolyte and other electrolytes. (a) Ragone plot of the EC systems based on the molten salt electrolyte and other electrolytes. (b) Radar plot of the molten salt electrolyte and other electrolytes in terms of safety, ionic conductivity, price, and energy densities of the corresponding EC device as quantified by Table S5 (ESI†).

advantage of higher electrode energy densities compared with other EC systems.

$$E_{\text{electrode}} = \frac{1}{2}CU^2 \quad (4)$$

where $E_{\text{electrode}}$ is the energy density, C is the specific capacitance of an EC calculated based on the active material mass in the electrodes, and U is the operating voltage.

It is worth noting that electrolytes also serve as active materials in ECs, whose effect on energy densities is a commonly overlooked parameter. Theoretically, the number of free ions in the electrolyte should match the capacitances of the electrodes to achieve the maximum device energy density (eqn (5)).[63] Since the solvent-free molten salt electrolyte has higher salt molality, its energy density (107 W h kg^{-1}) is higher than that of aqueous (15–80 W h kg^{-1}), ionic liquid (40–80 W h kg^{-1}), and organic systems (10–20 W h kg^{-1}) (eqn (6)).[60–66]

$$\frac{1}{E} = \frac{1}{E_{\text{electrode}}} + \frac{1}{E_{\text{electrolyte}}} \quad (5)$$

$$E_{\text{electrolyte}} = \frac{1}{2}\alpha n m_0 FU \quad (6)$$

where $E_{\text{electrolyte}}$ is the energy density of an EC calculated based on the electrolyte mass, α represents the fraction of total salt removed from the bulk electrolyte upon complete charging, n refers to the charge number of the adsorbed ion, m_0 is the

Table 1 Properties of other inorganic molten salt electrolytes and performance of the corresponding MS-EC devices

Composition[a]		$AlCl_3$–NaCl	$AlCl_3$–LiCl	LiBr–CsBr	LiBr–KBr–CsBr	LiI–CsI	LiI–KI–CsI
Melting point (MP) (°C)		126[31]	136[31]	283[67]	237[67]	217[68]	204[68]
Ionic conductivity (S cm^{-1})	MP + 20 °C	0.19	0.18	0.78	0.65	0.52	0.49
	MP + 50 °C	0.24	0.22	0.95	0.84	0.80	0.70
	MP + 100 °C	0.32	0.30	1.23	1.09	1.08	0.96
Operating voltage (V)		2.0	2.0	2.6	2.6	2.4	2.4
Specific capacitance[b] (F g^{-1})		297	292	277	268	379	340
Energy density[c] (W h kg^{-1})		41.3	40.6	65.0	63.0	75.9	68.1

[a] The molar ratios of the components are listed as follows: $AlCl_3$–NaCl (0.60 : 0.40), $AlCl_3$–LiCl (0.60 : 0.40), LiBr–CsBr (0.62 : 0.38), LiBr–KBr–CsBr (0.56 : 0.19 : 0.25), LiI–CsI (0.66 : 0.34), and LiI–KI–CsI (0.62 : 0.10 : 0.28). [b] Symmetric devices were fabricated. The electrode specific capacitances are calculated based on the CV curves at a scan rate of 20 mV s^{-1}. The working temperatures were 20 °C higher than the melting points of the electrolytes. [c] The energy densities are calculated based on the active material masses in the electrode.

initial salt molality in the electrolyte, and F is Faraday's constant; E is the energy density of an EC calculated based on the mass of the electrodes and the electrolyte.

Next to the observed superior energy densities, the inorganic molten salt electrolyte has industrial advantages of relatively low price, non-flammability, and non-toxicity. Consequently, it is an attractive choice for ECs based on its advantages in various aspects (Fig. 5b and Table S5, ESI†).

The universal application of suitable molten salts for EC systems was also confirmed. The properties of the salt mixtures consisting of common anions are shown in Table S6 (ESI†). The high melting points of the salt mixtures consisting of fluoride, chloride, and carbonate ions may cause increased self-discharge rates and operation and maintenance costs. Meanwhile, the electrochemical windows of the salt mixtures consisting of the nitrate ions (~1.6 V) are relatively narrow, leading to low energy and power densities of the device. The high corrosiveness of the molten hydroxide mixtures makes it unsuitable as an alternative electrolyte. In contrast, mixtures of salts consisting of chloroaluminate ions, bromine ions, and iodine ions demonstrate low melting points, wide electrochemical windows, and low corrosiveness, which were considered candidates for electrolytes for MS-ECs. The properties of some representative molten salt systems and the performance of the corresponding MS-EC devices are shown in Table 1. All the salt mixtures demonstrated high ionic conductivity (0.19–1.23 S cm^{-1}) with relatively wide electrochemical windows (2.0–2.6 V). In particular, the AC electrode presented a specific capacitance of 379 F g^{-1} in the LiI–CsI electrolyte at a scan rate of 20 mV s^{-1} in the voltage range of 0–2.4 V at 230 °C. The corresponding MS-EC achieved an ultrahigh energy density of 75.9 W h kg^{-1} (Fig. S32, ESI†). The melting points of the molten salts ranged from 126 °C to 283 °C, which qualifies these MS-ECs to be employed in different high-temperature application environments. Furthermore, considering that some specific inorganic molten salts are compatible with molten alkali metals, it is also likely to achieve even higher device energy densities when assembling Li-ion and Na-ion hybrid ECs.

Conclusions

In summary, we developed high-performance MS-ECs with electrodes synthesized from commercial AC. An ultrahigh specific capacitance of 419 F g^{-1} was achieved with the employed $AlCl_3$–NaCl–LiCl electrolyte, which can be attributed to the physisorption–chemisorption combined energy storage mechanism under electrolyte nanoconfinement. The corresponding device demonstrated an energy density of 50.4 W h kg^{-1} at a power density of 1.1 kW kg^{-1} at 125 °C. Negligible capacitance fade was observed after 10 000 cycles at a current density of 5 A g^{-1}. The self-discharge of the MS-ECs was revealed to be influenced by CR and diffusion-controlled mechanisms, and long-duration energy storage was accomplished by cooling down the electrolyte to its solid state. More importantly, the applicability of various types of inorganic molten salts with different properties was verified, which is expected to broaden the application field of ECs.

Experimental

Materials

AC was purchased from Fuzhou Yihuan Carbon Co., Ltd (Fuzhou, China). Carbon black was purchased from Hefei Kejing Co., Ltd (Hefei, China). Glass microfiber filters (Whatman 934-AH) were used as separators.

Electrode preparation

AC, carbon black (CB), polytetrafluoroethylene (PTFE) preparation (60 wt% dispersion in H_2O), and ethanol were mixed, processed into a thin slice, and pressed into two molybdenum meshes. The electrode was dried in an oven at 60 °C overnight before use. The weight ratio of AC, CB, and PTFE was 8 : 1 : 1. The active material loading was around 10–20 mg cm^{-2}, depending on the thickness of the AC electrode.

Electrolyte preparation

The $AlCl_3$–NaCl–LiCl electrolyte was prepared in an argon-filled glove box (Etelux, Lab2000). $AlCl_3$, NaCl, and LiCl powders were mixed with a molar ratio of 0.6 : 0.2 : 0.2. The mixture was heated in an alumina crucible to 150 °C for 12 h. The melts, which were clear and colorless, were poured out carefully and collected. Other electrolytes were prepared similarly. The preparation temperatures were adjusted according to the approximate melting points of molten salts.

Device assembly

Firstly, glass seals were applied between the Ta wires and the stainless-steel case. Secondly, the electrolyte was filled in the stainless-steel case and was heated to 180 °C. The electrodes were welded to the Ta wires and were immersed in the electrolyte. The first two steps were performed in the argon-filled glove box. Finally, the device was cooled to ambient temperature and taken out to ambient air. Laser welding was quickly applied at the threaded connection to ensure air tightness.

Materials characterization

The microstructures of the samples were analyzed by SEM (MERLIN Compact Zeiss) and TEM (Jeol-2010, Japan). The surface areas, adsorption and desorption isotherms, and pore size distributions of the samples were investigated using an analyzer (Micromeritics ASAP 2460) at 87 K of argon. Phase identifications of the samples were analyzed using XPS (Amicus Budget) and XRD (D-Max-2500 Rigaku XRD Analyzer). Raman spectra were recorded using a 532 nm laser (LabRAM HR Evolution). The DSC curves were obtained using an analyzer (TA-DSC25) with a heating rate of 10 K min^{-1}.

Electrochemical characterization

The electrochemical performance of the AC electrode was tested using a three-electrode method in a muffle furnace (MTI) in the glove box. The AC electrode, Ta foil, and Al foil were used as the working electrode, the counter electrode, and the reference electrode, respectively. Cyclic voltammetry measurements were conducted on an electrochemical workstation (CHI 660e). MS-EC devices were tested in a muffle furnace (MTI) in ambient air. CV and galvanostatic charge/discharge (GCD) tests were performed on the electrochemical workstation in the two-electrode mode. Electrolyte conductivities, device impedances, and self-discharge profiles were measured with an electrochemical workstation (Metrohm Autolab). Electrolyte conductivities were measured *via* the FRA impedance potentiostatic mode. Two Ta foils were applied as electrodes, and the resistances were recorded when the imaginary part of the impedance was equal to zero. Device impedances were measured *via* the FRA impedance potentiostat in the frequency range of 100 kHz to 10 mHz. Self-discharge measurements were tested after the MS-ECs were charged to a specific voltage with a current density of 1 A g^{-1}. The devices were held at 2.0 V for 2 h (unless exceptions are stated) to facilitate a more uniform CR before the open-circuit voltage tests. In order to test the long-duration self-discharge rates, the device was charged to 2.0 V after being cycled for 100 cycles and held at 2.0 V for 2 h at 125 °C. Then the device was taken out from the muffle furnace and placed at room temperature for around 25 days. Finally, the device was heated to 125 °C and cycled again. The cycling performance was tested using a battery test system (LAND, 2001CT).

Author contributions

Kuangyu Wang: conceptualization, methodology, software, investigation, and writing – original draft. Ziyao Chen: conceptualization, methodology, software, investigation, and writing – original draft. Kai Liu: conceptualization, methodology, investigation, and writing – original draft. Cheng Yang: investigation. Haitian Zhang: investigation. Yulong Wu: investigation. Yuanzheng Long: investigation. Hanlin Liu: software and writing – review & editing. Yang Jin: writing – original draft. Meicheng Li: writing – original draft. Hui Wu: conceptualization, writing – original draft, supervision, and funding acquisition.

Conflicts of interest

A patent has been applied on behalf of Tsinghua University. H. W., K. W., Z. C., and K. L. are listed as inventors. Other authors declare that they have no competing financial interests.

Acknowledgements

This work was supported by the Basic Science Center Program of the National Natural Science Foundation of China (NSFC) under Grant No. 51788104 and the Beijing Natural Science Foundation under Grant No. JQ19005.

Notes and references

1 P. Simon and Y. Gogotsi, *Nat. Mater.*, 2008, **7**, 845–854.
2 P. Simon and Y. Gogotsi, *Nat. Mater.*, 2020, **19**, 1151–1163.
3 W. Gu and G. Yushin, *Wiley Interdiscip. Rev.: Energy Environ.*, 2014, **3**, 424–473.
4 Q. Zhu, D. Zhao, M. Cheng, J. Zhou, K. A. Owusu, L. Mai and Y. Yu, *Adv. Energy Mater.*, 2019, **9**, 1901081.
5 F. Béguin, V. Presser, A. Balducci and E. Frackowiak, *Adv. Mater.*, 2014, **26**, 2219–2251.
6 S. Najib and E. Erdem, *Nanoscale Adv.*, 2019, **1**, 2817–2827.
7 S. Zhang and N. Pan, *Adv. Energy Mater.*, 2015, **5**, 1401401.
8 W. Raza, F. Ali, N. Raza, Y. Luo, K. H. Kim, J. Yang, S. Kumar, A. Mehmood and E. E. Kwon, *Nano Energy*, 2018, **52**, 441–473.
9 N. Choudhary, C. Li, J. Moore, N. Nagaiah, L. Zhai, Y. Jung and J. Thomas, *Adv. Mater.*, 2017, **29**, 1605336.
10 Y. Shao, M. F. El-Kady, J. Sun, Y. Li, Q. Zhang, M. Zhu, H. Wang, B. Dunn and R. B. Kaner, *Chem. Rev.*, 2018, **118**, 9233–9280.
11 A. Eftekhari, *Energy Storage Mater.*, 2017, **9**, 47–69.
12 C. Zhong, Y. Deng, W. Hu, J. Qiao, L. Zhang and J. Zhang, *Chem. Soc. Rev.*, 2015, **44**, 7484–7539.
13 L. Yu and G. Z. Chen, *Front. Chem.*, 2019, **7**, 272.
14 K. Wang, K. Jiang, B. Chung, T. Ouchi, P. J. Burke, D. A. Boysen, D. J. Bradwell, H. Kim, U. Muecke and D. R. Sadoway, *Nature*, 2014, **514**, 348–350.
15 H. Yin, B. Chung, F. Chen, T. Ouchi, J. Zhao, N. Tanaka and D. R. Sadoway, *Nat. Energy*, 2018, **3**, 127–131.
16 R. A. Guidotti and P. Masset, *J. Power Sources*, 2006, **161**, 1443–1449.
17 J. Wang, X. Zhang, W. Chu, S. Liu and H. Yu, *Chem. Commun.*, 2019, **55**, 2138–2141.

18 Y. Sato, *ECS Trans.*, 2010, **33**, 145–157.
19 M. Walz and D. van der Spoel, *Commun. Chem.*, 2021, **4**, 9.
20 T. Murakami, T. Nohira, Y. H. Ogata and Y. Ito, *Electrochem. Solid-State Lett.*, 2005, **8**, 8–11.
21 K. Liu, J. Lang, M. Yang, J. Xu, B. Sun, Y. Wu, K. Wang, Z. Zheng, Z. Huang, C. Wang, H. Wu, Y. Jin and Y. Cui, *Matter*, 2020, **3**, 1714–1724.
22 K. Wang, K. Liu, C. Yang, Z. Chen, H. Zhang, Y. Wu, Y. Long, Y. Jin, X. He and H. Wu, *Energy Storage Mater.*, 2022, **48**, 356–365.
23 J. Tu, J. Wang, H. Zhu and S. Jiao, *J. Alloys Compd.*, 2020, **821**, 153285.
24 S. Rashidi, N. Karimi, B. Sunden, K. C. Kim, A. G. Olabi and O. Mahian, *Prog. Energy Combust. Sci.*, 2022, **88**, 100966.
25 S. Koohi-Kamali, V. V. Tyagi, N. A. Rahim, N. L. Panwar and H. Mokhlis, *Renew. Sustain. Energy Rev.*, 2013, **25**, 135–165.
26 M. Farhadi and O. Mohammed, *IEEE Trans. Ind. Appl.*, 2016, **52**, 1953–1962.
27 X. Lin, M. Salari, L. M. R. Arava, P. M. Ajayan and M. W. Grinstaff, *Chem. Soc. Rev.*, 2016, **45**, 5848–5887.
28 S. Hajiaghasi, A. Salemnia and M. Hamzeh, *J. Energy Storage*, 2019, **21**, 543–570.
29 L. Kouchachvili, W. Yaïci and E. Entchev, *J. Power Sources*, 2018, **374**, 237–248.
30 H. Wang, H. Niu, H. Wang, W. Wang, X. Jin, H. Wang, H. Zhou and T. Lin, *J. Power Sources*, 2021, **482**, 228986.
31 Y. Sato and T. Ejima, *Proc. Electrochem. Soc.*, 1984, **84–2**, 121–132.
32 S. W. Prömper and W. Frank, *Acta Crystallogr., Sect. E: Crystallogr. Commun.*, 2017, **73**, 1426–1429.
33 G. Torsi, G. Mamantov and G. M. Begun, *Inorg. Nucl. Chem. Lett.*, 1970, **6**, 553–560.
34 K. Balasubrahmanyam and L. Nanis, *J. Chem. Phys.*, 1965, **42**, 676–680.
35 J. Tu, S. Wang, S. Li, C. Wang, D. Sun and S. Jiao, *J. Electrochem. Soc.*, 2017, **164**, A3292–A3302.
36 M. Salanne, L. J. A. Siqueira, A. P. Seitsonen, P. A. Madden and B. Kirchner, *Faraday Discuss.*, 2012, **154**, 171–188.
37 H. Wang, D. Xu, G. Jia, Z. Mao, Y. Gong, B. He, R. Wang and H. J. Fan, *Energy Storage Mater.*, 2020, **25**, 114–123.
38 S. Zhang, J. Zhang, Y. Zhang and Y. Deng, *Chem. Rev.*, 2017, **117**, 6755–6833.
39 R. Hayes, G. G. Warr and R. Atkin, *Chem. Rev.*, 2015, **115**, 6357–6426.
40 R. Futamura, T. Iiyama, Y. Takasaki, Y. Gogotsi, M. J. Biggs, M. Salanne, J. Ségalini, P. Simon and K. Kaneko, *Nat. Mater.*, 2017, **16**, 1225–1232.
41 S. Fleischmann, Y. Zhang, X. Wang, P. T. Cummings, J. Wu, P. Simon, Y. Gogotsi, V. Presser and V. Augustyn, *Nat. Energy*, 2022, **7**, 222–228.
42 N. N. Rajput, J. Monk, R. Singh and F. R. Hung, *J. Phys. Chem. C*, 2012, **116**, 5169–5181.
43 R. Singh, J. Monk and F. R. Hung, *J. Phys. Chem. C*, 2011, **115**, 16544–16554.
44 S. Chen, Y. Liu, H. Fu, Y. He, C. Li, W. Huang, Z. Jiang and G. Wu, *J. Phys. Chem. Lett.*, 2012, **3**, 1052–1055.
45 S. Fleischmann, J. B. Mitchell, R. Wang, C. Zhan, D. E. Jiang, V. Presser and V. Augustyn, *Chem. Rev.*, 2020, **120**, 6738–6782.
46 C. Choi, D. S. Ashby, D. M. Butts, R. H. DeBlock, Q. Wei, J. Lau and B. Dunn, *Nat. Rev. Mater.*, 2020, **5**, 5–19.
47 P. Bhauriyal, A. Mahata and B. Pathak, *Phys. Chem. Chem. Phys.*, 2017, **19**, 7980–7989.
48 Q. Dou, C. Lian, S. Lei, J. Chen, H. Liu and X. Yan, *Energy Storage Mater.*, 2019, **18**, 253–259.
49 S. Dsoke, B. Fuchs, E. Gucciardi and M. Wohlfahrt-Mehrens, *J. Power Sources*, 2015, **282**, 385–393.
50 S. Vaquero, J. Palma, M. Anderson and R. Marcilla, *J. Electrochem. Soc.*, 2013, **160**, A2064–A2069.
51 M. Haque, Q. Li, A. D. Smith, V. Kuzmenko, E. Köhler, P. Lundgren and P. Enoksson, *Electrochim. Acta*, 2018, **263**, 249–260.
52 L. H. Hess, N. Fulik, J. Röhner, E. Zhang, S. Kaskel, E. Brunner and A. Balducci, *Energy Storage Mater.*, 2021, **37**, 501–508.
53 B. E. Conway, W. G. Pell and T. C. Liu, *J. Power Sources*, 1997, **65**, 53–59.
54 M. Haque, Q. Li, A. D. Smith, V. Kuzmenko, P. Rudquist, P. Lundgren and P. Enoksson, *J. Power Sources*, 2020, **453**, 227897.
55 M. Haque, Q. Li, C. Rigato, A. Rajaras, A. D. Smith, P. Lundgren and P. Enoksson, *J. Power Sources*, 2021, **485**, 229328.
56 Z. Wang, X. Chu, Z. Xu, H. Su, C. Yan, F. Liu, B. Gu, H. Huang, D. Xiong, H. Zhang, W. Deng, H. Zhang and W. Yang, *J. Mater. Chem. A*, 2019, **7**, 8633–8640.
57 T. Tevi, H. Yaghoubi, J. Wang and A. Takshi, *J. Power Sources*, 2013, **241**, 589–596.
58 M. Xia, J. Nie, Z. Zhang, X. Lu and Z. L. Wang, *Nano Energy*, 2018, **47**, 43–50.
59 K. Fic, G. Lota and E. Frackowiak, *Electrochim. Acta*, 2010, **55**, 7484–7488.
60 X. Sun, X. Zhang, H. Zhang, D. Zhang and Y. Ma, *J. Solid State Electrochem.*, 2012, **16**, 2597–2603.
61 Z. Sun, M. Zheng, H. Hu, H. Dong, Y. Liang, Y. Xiao, B. Lei and Y. Liu, *Chem. Eng. J.*, 2018, **336**, 550–561.
62 Z. Qiu, Y. Wang, X. Bi, T. Zhou, J. Zhou, J. Zhao, Z. Miao, W. Yi, P. Fu and S. Zhuo, *J. Power Sources*, 2018, **376**, 82–90.
63 A. Brandt and A. Balducci, *J. Power Sources*, 2014, **250**, 343–351.
64 E. Mourad, L. Coustan, P. Lannelongue, D. Zigah, A. Mehdi, A. Vioux, S. A. Freunberger, F. Favier and O. Fontaine, *Nat. Mater.*, 2017, **16**, 446–454.
65 Q. D. Nguyen, J. Patra, C. Te Hsieh, J. Li, Q. F. Dong and J. K. Chang, *ChemSusChem*, 2019, **12**, 449–456.
66 R. Francke, D. Cericola, R. Kötz, D. Weingarth and S. R. Waldvogel, *Electrochim. Acta*, 2012, **62**, 372–380.
67 A. Redkin, I. Korzun, T. Yaroslavtseva, O. Reznitskikh and Y. Zaikov, *J. Therm. Anal. Calorim.*, 2017, **128**, 621–626.
68 J. Songster and A. D. Pelton, *J. Phase Equilibria*, 1991, **12**, 511–537.